Improvements in Level Set Segmentation of 3D Small Animal Imagery

Jeffery R. Price[a], Deniz Aykac[a], Jonathan Wall[b]

[a] Oak Ridge National Laboratory, Oak Ridge, TN
[b] University of Tennessee, Knoxville, TN

ABSTRACT

In this paper, we investigate several improvements to region-based level set algorithms in the context of segmenting x-ray CT data from pre-clinical imaging of small animal models. We incorporate a recently introduced signed distance preserving term into a region-based level set model and provide formulas for a semi-implicit finite difference implementation. We illustrate some pitfalls of topology preserving level sets and introduce the concept of connectivity preservation as a potential alternative. We illustrate the benefits of these improvements on phantom and real data.

Keywords: Level sets, active contours, segmentation, topology preserving level sets

1. INTRODUCTION

The study of small animal models has increasingly become an important vehicle for elucidating human disease mechanisms. Mice in particular have received notable attention, primarily because of substantial similarities between the mouse and human genome as well as the relative ease with which mice can be genetically manipulated.[1] Our efforts in this paper are motivated by the study of a transgenic mouse model of AA-amyloidosis using 3D anatomic and functional imaging.[2] Our goal is to develop improved methods for semi-automatic segmentation of the spleen using contrast-enhanced microCT data. The mouse spleen, however, is challenging to segment. An example slice from a volumetric data set is shown in Fig. 1. Even with the aid of blood-pool contrast-enhancement, the boundaries are weak and the interior is inhomogeneous due to the presence of follicles which contain no blood.

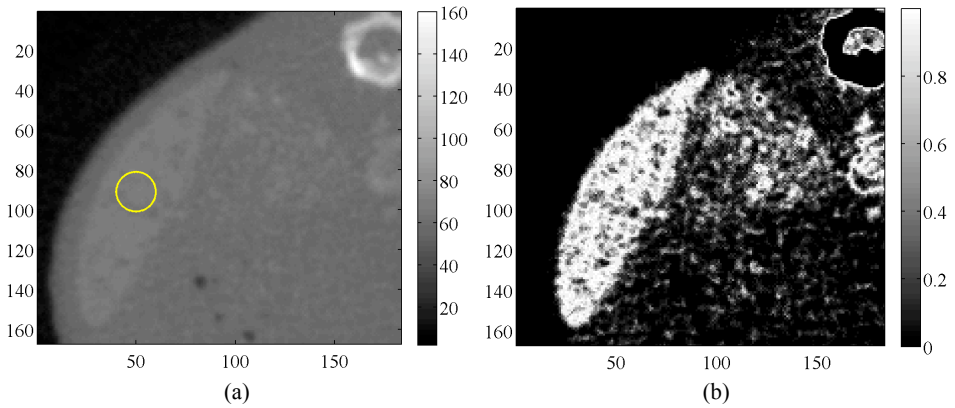

Figure 1. Example of raw data and corresponding likelihood image. (a) Grayscale image of raw CT data containing a portion of the spleen. The small circle in the spleen region surrounds a manually marked seed point used to initialize the semi-automatic segmentation process. (b) Likelihood image corresponding to raw data from (a). A two-component Gaussian mixture is estimated from the seed region. The resulting higher mean component represents the spleen blood pool and is used to compute the likelihood image (see Section 3.1).

Correspondence: J. Price, pricejr@ornl.gov, 865-574-5743

Building upon our earlier work,[3,4] we explore several low-level improvements to level set algorithms in the context of segmenting 3D small animal CT imagery. The specific contributions of this paper are as follows.

- We introduce the signed distance preserving term of Li *et al.*[5] into the Chan-Vese region-based level set formulation and provide a 3D, semi-implicit finite difference implementation.
- We demonstrate the improved performance of the semi-implicit scheme relative to an explicit scheme.
- We demonstrate the improvement provided by the signed distance term and quantify the additional computational burden, which is minimal relative to periodic reinitialization.
- We illustrate some pitfalls of topology preserving level sets and introduce *connectivity preservation* as a potential remedy.

For notational convenience, we will sometimes refer to the signed distance preserving term as the γ-term (see Section 2).

The remainder of this paper is organized as follows. In Section 2, we give the region-based level set formulation, based on the Chan-Vese[6] model and include the signed distance preserving term of Li *et al.*. We also present in this section a semi-implicit finite difference implementation and discuss our convergence criteria. In Section 3, we describe how we use the model for segmenting the mouse spleen and present the concept of connectivity preservation. We then present some experimental results in Section 4 and close in Section 5.

2. LEVEL SET FORMULATION AND NUMERICAL IMPLEMENTATION

We seek a contour C such that the region of interest is contained inside C. In the level set formulation,[7] this contour C is defined implicitly as the zero level set of a function $f : \Omega \to \mathbb{R}$ where $\Omega \subset \mathbb{R}^3$ for volumetric data. The aim then is to find an optimal level set function f according to some pre-defined criteria. The contour is formally defined as $C = \{(x, y, z) : f(x, y, z) = 0\}$. We define the region inside the surface by $f(x, y, z) > 0$ and call it R_1; the region outside, R_2, is where $f(x, y, z) \leq 0$. For notational convenience henceforth, we will use $\mathbf{s} \equiv (x, y, z)$ for the spatial coordinates when needed. However, we will often leave implicit the dependence on the spatial coordinates, i.e., we will use $f \equiv f(x, y, z) \equiv f(\mathbf{s})$.

2.1. Formulation

Because of the poor contrast and unclear edges in our data (see Fig. 1), we adopt the region-based level set approach first suggested by Chan and Vese.[6] In that model, as in almost all level set models, it is assumed that the level set function f is a signed distance function, i.e., that $|\nabla f| = 1$. However, this important constraint is not enforced by the evolution itself, but rather by periodic reinitialization which is often performed by solving the following evolution equation*

$$\frac{\partial f}{\partial t} = \text{sign}(f)(1 - |\nabla f|) \tag{1}$$

with an appropriate upwind finite difference scheme.[9] Unfortunately, when such reinitialization should be performed and with what parameters (time step and number of iterations) are not well defined quantities. A recently proposed technique by Li *et al.*,[5] however, potentially removes this need for reinitialization; the constraint that $|\nabla f| = 1$ is incorporated directly into the energy functional. With this modification to the Chan-Vese formulation, the energy functional $J(f)$ we seek to minimize can be expressed

$$J(f) = \lambda_1 \int (u - \mu_1)^2 H_\epsilon(f) d\mathbf{s} + \lambda_2 \int (u - \mu_2)^2 \big(1 - H_\epsilon(f)\big) d\mathbf{s} + \nu \int \delta_\epsilon(f) |\nabla f| d\mathbf{s} + \gamma \int \frac{1}{2} (|\nabla f| - 1)^2 d\mathbf{s}, \tag{2}$$

where $u \equiv u(\mathbf{s})$ is the data being segmented, $H_\epsilon(\cdot)$ is a regularized Heaviside step function, $\delta_\epsilon(\cdot)$ is a regularized Dirac function, and μ_1 and μ_2 represent the averages of u in R_1 (inside the contour) and R_2 (outside the

*We note that fast distance transforms[8] are an alternative to iterative reinitialization via Eq. (1).

contour), respectively. Intuitively, the first two terms of $J(f)$ – weighted by λ_1 and λ_2 – represent the image-based component and minimizing them implies that u is approximately homogeneous both in R_1 and in R_2. The third term, weighted by ν, represents the smoothness of the contour and the fourth term, weighted by γ, represents the signed distance preserving term of Li *et al.*, which, for convenience, we refer to as the γ-term.

The energy functional is minimized using an Euler-Lagrange approach with artificial time t, resulting in the following PDE:

$$\begin{aligned}\frac{\partial f}{\partial t} &= \delta_\epsilon(f)\big(\lambda_2(u-\mu_2)^2 - \lambda_1(u-\mu_1)^2\big) + \delta_\epsilon(f)\big(\nu \operatorname{div}\Big(\frac{\nabla f}{|\nabla f|}\Big)\big) + \gamma\big(\nabla^2 f - \operatorname{div}\Big(\frac{\nabla f}{|\nabla f|}\Big)\big) \\ &= \delta_\epsilon(f)\big(\lambda_2(u-\mu_2)^2 - \lambda_1(u-\mu_1)^2\big) + \big(\nu\delta_\epsilon(f) - \gamma\big) \operatorname{div}\Big(\frac{\nabla f}{|\nabla f|}\Big) + \gamma(\nabla^2 f),\end{aligned} \tag{3}$$

where ∇^2 represents the Laplacian operator and where $\partial f/\partial t = 0$ for the optimal f.

2.2. Numerical Implementation

We use D_+^x, D_-^x, and D_c^x to represent first-order forward, backward, and central difference operators, respectively, in the x direction; similar definitions apply for the y and z directions. We let $f_{i,j,k}$ represent the discretization of $f(x,y,z)$, but, for notational convenience, we drop the subscripts when they are centered, i.e., $f \equiv f_{i,j,k}$ but $f_{i+1} \equiv f_{i+1,j,k}$. Hence, $D_+^x f = f_{i+1} - f$, $D_-^x f = f - f_{i-1}$, and $D_c^x f = f_{i+1} - f_{i-1}$. We let d represent the dimensionality of the data, e.g., $d = 2$ for image data and $d = 3$ for volumetric data. We use the following non-compact regularizations for the Heaviside and Dirac functions:

$$H_\epsilon(a) = \frac{1}{2} + \frac{1}{\pi}\tan^{-1}\Big(\frac{a}{\epsilon}\Big) \quad \text{and} \quad \delta_\epsilon(a) = \frac{\epsilon^2}{\epsilon^2 + a^2}$$

with $\epsilon = 1$. We note that $\delta_\epsilon(a)$ is normalized so that $\delta_\epsilon(0) = 1$.

To discretize Eq. (3), we adopt a semi-implicit finite difference scheme like that of Vese and Chan[10] and described as follows. We first consider the divergence term, where

$$\operatorname{div}\Big(\frac{\nabla f}{|\nabla f|}\Big) = \frac{\partial}{\partial x}\Big(\frac{\partial f/\partial x}{|\nabla f|}\Big) + \frac{\partial}{\partial y}\Big(\frac{\partial f/\partial y}{|\nabla f|}\Big) + \frac{\partial}{\partial z}\Big(\frac{\partial f/\partial z}{|\nabla f|}\Big). \tag{4}$$

For the x component of Eq. (4), we use the following discrete approximation

$$\begin{aligned}\frac{\partial}{\partial x}\Big(\frac{\partial f/\partial x}{|\nabla f|}\Big) \to \hat{\Delta}_x f &= D_-^x \circ \left(\frac{D_+^x f}{\sqrt{(D_+^x f)^2 + (D_c^y f)^2 + (D_c^z f)^2}}\right) \\ &= \frac{D_+^x f}{\sqrt{(D_+^x f)^2 + (D_c^y f)^2 + (D_c^z f)^2}} - \frac{D_+^x f_{i-1}}{\sqrt{(D_+^x f_{i-1})^2 + (D_c^y f_{i-1})^2 + (D_c^z f_{i-1})^2}} \\ &= C_1(f_{i+1} - f) - C_2(f - f_{i-1}),\end{aligned} \tag{5}$$

where

$$C_1 = \frac{1}{\sqrt{(D_+^x f)^2 + (D_c^y f)^2 + (D_c^z f)^2}} \tag{6}$$

and

$$C_2 = \frac{1}{\sqrt{(D_+^x f_{i-1})^2 + (D_c^y f_{i-1})^2 + (D_c^z f_{i-1})^2}}. \tag{7}$$

Using the same approach for the y and z components of Eq. (4), we get

$$\begin{aligned}\operatorname{div}\Big(\frac{\nabla f}{|\nabla f|}\Big) \to \hat{\Delta} f &= C_1 f_{i+1} + C_2 f_{i-1} + C_3 f_{j+1} + C_4 f_{j-1} + C_5 f_{k+1} + C_6 f_{k-1} + \sum_{l=1}^{2d} C_l f \\ &= \mathcal{D} - \mathcal{C} f\end{aligned} \tag{8}$$

for the complete approximation of Eq. (4), where we use $\mathcal{D}$ to represent the first six terms and $\mathcal{C}$ to represent the summation of the C_l terms.

We now consider the Laplacian term from Eq. (3), where

$$\nabla^2 f = \frac{\partial^2 f}{\partial x^2} + \frac{\partial^2 f}{\partial y^2} + \frac{\partial^2 f}{\partial z^2}. \tag{9}$$

We approximate the x component of the Laplacian using

$$\frac{\partial^2 f}{\partial x^2} \rightarrow D_-^x D_+^x f = f_{i+1} - 2f + f_{i-1}. \tag{10}$$

Using the same scheme for the y and z components yields

$$\begin{aligned} \nabla^2 f \rightarrow \hat{\nabla}^2 f &= f_{i+1} + f_{i-1} + f_{j+1} + f_{j-1} + f_{k+1} + f_{k-1} - (2d)f \\ &= \mathcal{L} - (2d)f \end{aligned} \tag{11}$$

for the complete approximation of Eq. (9), where we use $\mathcal{L}$ to represent the first six terms.

Using the spatial discretizations from Eq. (8) and Eq. (11), we discretize the time derivative from Eq. (3) using

$$\frac{\partial f}{\partial t} \rightarrow \frac{f^{n+1} - f^n}{\tau} = \delta_\epsilon(f^n)\big(\lambda_2(u-\mu_2^n)^2 - \lambda_1(u-\mu_1^n)^2\big) + \big(\nu\delta_\epsilon(f^n) - \gamma\big)\hat{\Delta} f^n + \gamma\hat{\nabla}^2 f^n, \tag{12}$$

where the superscript indicates the discrete time step. We define

$$\mathcal{I}^n = \lambda_2(u-\mu_2^n)^2 - \lambda_1(u-\mu_1^n)^2, \tag{13}$$

where μ_1^n and μ_2^n are given by

$$\mu_1^n = \frac{\sum_{i,j,k} f^n H(f^n)}{\sum_{i,j,k} H(f^n)} \tag{14}$$

and

$$\mu_2^n = \frac{\sum_{i,j,k} f^n\big(1 - H(f^n)\big)}{\sum_{i,j,k}\big(1 - H(f^n)\big)}. \tag{15}$$

We use the results of Eq. (8) and Eq. (11) and, for the semi-implicit scheme, we substitute f^{n+1} on the right hand side of Eq. (12) for f^n wherever it appears linearly without spatial shifting. This yields

$$\frac{f^{n+1} - f^n}{\tau} = \delta_\epsilon(f^n)\mathcal{I}^n + \big(\nu\delta_\epsilon(f^n) - \gamma\big)(\mathcal{D}^n - \mathcal{C}f^{n+1}) + \gamma\big(\mathcal{L}^n - (2d)f^{n+1}\big). \tag{16}$$

Rearranging Eq. (16) finally leads us to our level set update equation:

$$f^{n+1} = \frac{f^n + \tau\delta_\epsilon(f)\mathcal{I}^n + \tau\big(\nu\delta_\epsilon(f) - \gamma\big)\mathcal{D}^n + \tau\gamma\mathcal{L}^n}{1 + \tau 2d\gamma + \tau\mathcal{C}^n\big(\nu\delta_\epsilon(f) - \gamma\big)}. \tag{17}$$

2.3. Computational Cost of the Signed Distance Term

We can quantify the additional computation introduced by the γ-term as follows. We first note the $(\nu\delta_\epsilon(f) - \gamma)$ term in both the numerator and denominator; this incurs one ADD operation per grid point per iteration. Expanding the $\mathcal{D}^n$ and $\mathcal{L}^n$ terms in the numerator, we find that $\tau\big(\nu\delta_\epsilon(f) - \gamma\big)\mathcal{D}^n + \tau\gamma\mathcal{L}^n$ can be written as the summation of six terms of the form $\tau f_{i+1}\big(\gamma + C_1(\nu\delta_\epsilon(f) - \gamma)\big)$. Hence, letting $d = 2$ or $d = 3$ represent the data dimensionality, the net result is that in the semi-implicit scheme of Eq. (17), the γ-term incurs a computational burden of only $2d + 1$ ADD operations per grid point per iteration. In contrast, the upwind implementation of the reinitialization evolution from Eq. (1) requires $d + 2$ ADDs, $4d + 2$ MULTs, and 2 SQRTs per grid point per iteration (of reinitialization); this ignores the burden of several max, min, sign, and conditionals.

2.4. Convergence

We adopt a simple mechanism to define convergence that is heuristic yet effective. We note that the shape of the object or objects being segmented changes (on a full pixel scale) from step n to $n+1$ only if some grid points of the level set function f change sign. We note, however, that there are often small scale oscillations in n that can cause a single point to change signs repeatedly. Hence, we count the number of new grid points (i.e., those that have not previously changed sign) that change sign on each iteration. If this number is zero (or below a threshold) for several successive time steps, we terminate the iteration. In our 2D results in Section 4, we define convergence to be 5 iterations where zero new points change sign.

3. APPLICATION TO THE MOUSE SPLEEN

In this section, we discuss some specifics of segmenting the contrast-enhanced, inhomogeneous mouse spleen using the region-based level set model described above.

3.1. Blood Pool Likelihood Image

Despite the use of a contrast agent, the spleen contrast is not sufficient to perform segmentation on the raw data. The spleen interior comprises two primary components, blood and follicles. X-ray contrast is produced using a venous contrast agent; hence the blood region appears relatively brighter than the follicles and other surrounding soft tissue, perhaps with the exception of some connected veins that also contain contrast agent and/or near-bone regions. In our semi-automatic approach, an interior point near the spleen middle is marked by the biologist or technician reviewing the reconstructed CT imagery. As shown in Fig. 1, we initialize the contour to a small circle (or sphere) around this seed point such that the circle contains both blood pool and follicle regions. We then estimate a two-component Gaussian mixture on the pixels (or voxels) in this region; the component with the higher mean is the blood pool. Letting the blood pool mean and standard deviation be represented by μ_b and σ_b, respectively, we compute a likelihood image as

$$u_{i,j,k} = \exp\Big(\frac{-(r_{i,j,k} - \mu_b)^2}{2\sigma_b^2}\Big) \tag{18}$$

where $r_{i,j,k}$ represents the raw image data. An example likelihood image computed in this fashion is shown in Fig. 1(b) and demonstrates the improved contrast of the spleen blood pool provided by this approach. We apply the segmentation algorithm(s) to these likelihood images rather than the raw data.

3.2. Connectivity Preserving Level Sets

The outer spleen surface in 3D is topologically equivalent to the sphere. Due to its arrangement in the mouse body relative to the CT scan direction, each transaxial slice of the spleen is also topologically equivalent to a circle. This leads us to consider the application of topology preserving level sets.[11]

As noted by Han *et al.*, topology in the level set segmentation cannot change unless a *non-simple* grid point of the level set function f changes sign from one iteration to the next. Consider the level set function at some grid point (i, j, k) that, according to the update equation, would change sign. Let $\mathcal{F}^n$ represent the number of connected foreground components and $\mathcal{B}^n$ the number of connected background components in the $3 \times 3 \times 3$ neighborhood around the point (i, j, k), where the foreground and background connectivities are appropriately dual. In topology preserving level sets, we allow (i, j, k) to change sign only if it is a *simple* point, meaning that both $\mathcal{F}^{n+1} = \mathcal{F}^n$ and $\mathcal{B}^{n+1} = \mathcal{B}^n$ if the point were to change sign. If (i, j, k) is not simple, we do not allow $f_{i,j,k}$ to change sign and instead set $f^{n+1}_{i,j,k} = \varepsilon\,\mathrm{sign}(f^n_{i,j,k})$, where ε is some small positive number. This topology check must be performed at every iteration for every grid point that would change sign according to the update equation. It can be performed quite efficiently via the computation of some topological numbers, but as we note below, the sheer number of such checks can be computationally demanding. Furthermore, the results of topology preservation, however, are not always desirable (see Figs. 4 and 5 later).

Even though the outer surface of the spleen is topologically equivalent to the sphere, we are using the enhanced blood pool to differentiate the spleen. This implies a region with interior holes because of the follicles. Hence, topology preservation is not necessarily appropriate. Instead, we expect our segmentation result (at least

initially) to be a single connected region, perhaps with holes. This leads us to propose *connectivity preservation*. Like topology, connectivity cannot change unless a grid point of f changes sign. Assuming, by convention, that the region of interest is the foreground region where $f_{i,j,k} > 0$, foreground connectivity will be preserved when $f_{i,j,k}$ changes sign only if $\mathcal{F}^{n+1} \leq \mathcal{F}_n$. We hence count the number of connected foreground components with and without the potential sign change. If the number of components stays the same or decreases, we allow the update, otherwise, we set $f^{n+1}_{i,j,k} = \varepsilon\,\mathrm{sign}(f^n_{i,j,k})$ as with topology preservation. Some illustrative examples of connectivity preservation are shown in Figs. 4 and 5 in Section 4.3.

4. EXPERIMENTAL RESULTS

Here we present experimental results illustrating the performance of the various algorithmic improvements described above, including the semi-implicit scheme, the signed distance term, and connectivity preservation. We conclude with some example results applied to mouse spleen data.

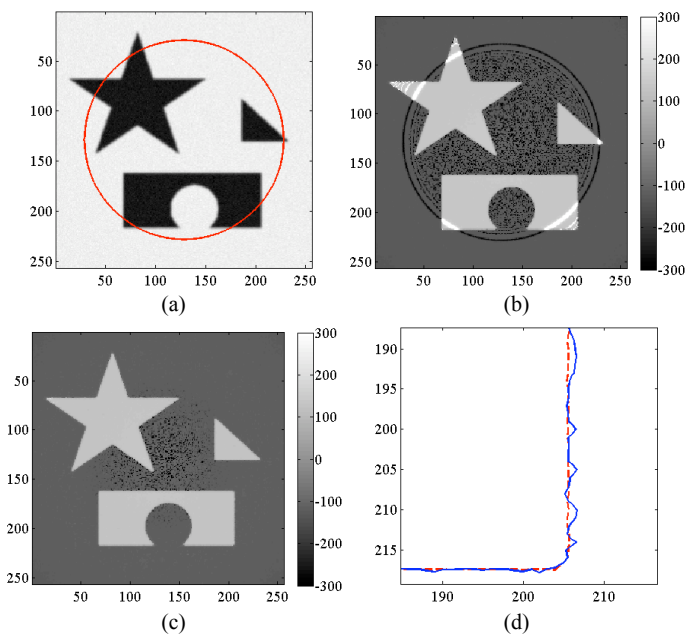

Figure 2. Comparison of explicit vs. semi-implicit finite difference schemes. (a) Level set function is initialized to signed distance function around the indicated contour. (b) Converged level set function after 368 iterations using explicit scheme. (c) Converged level set function after 367 iterations using semi-implicit scheme. (d) Zoom on resulting final contours, where the dashed line indicates the semi-implicit result. Note that the explicit result in (b) exhibits oscillations around the initialization which can also be observed in the corresponding contour in (d). Parameters were $\tau = 0.05$, $\nu = 0.01 \times 255^2$, $\lambda_1 = \lambda_2 = 1$, and $\gamma = 0$. We henceforth employ the semi-implicit scheme for all following results.

4.1. Semi-implicit vs. Explicit Scheme

We first consider the semi-implicit finite difference scheme of Eq. (17) relative to a more simple explicit scheme. Example results, with parameters noted in the caption, are illustrated in Fig. 2 on a phantom image. We note that the converged level set function of the explicit scheme in (b) exhibits strong oscillations about the initial contour. The converged level set function from the semi-implicit scheme is shown in (c) and exhibits negligible lingering oscillations from the initialization. As evident in (d), these oscillations have a detrimental effect on the smoothness of the resulting contour.

4.2. Signed Distance Term

We illustrate the improvements from the γ-term in Fig. 3. In (b), we show contours of the converged level set function at $\{-80, -40, 0, 40, 80\}$ without using the γ-term. These contours have collapsed onto one another,

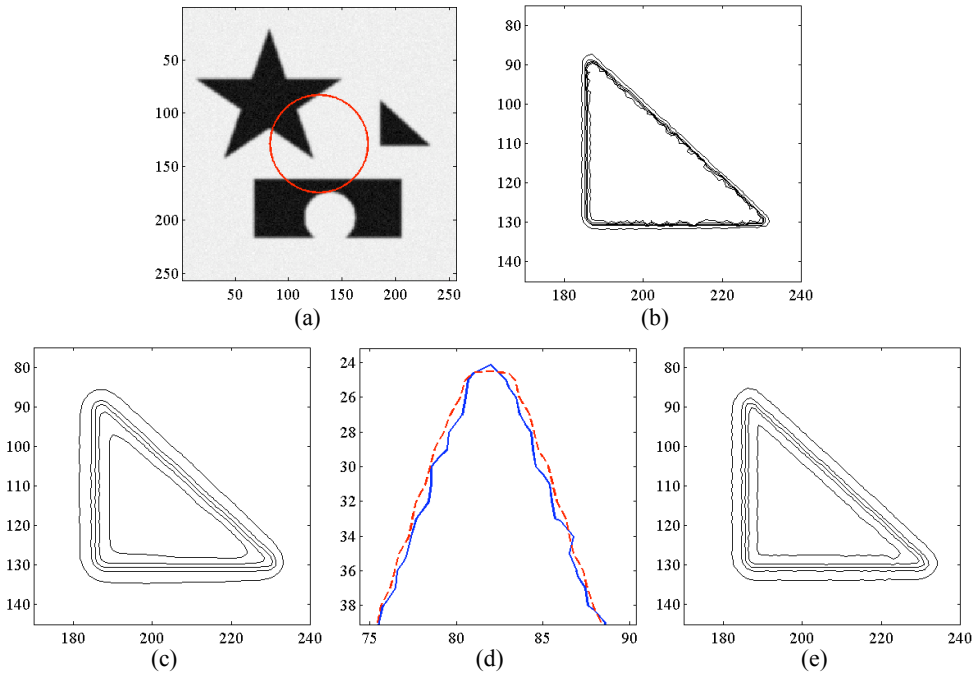

Figure 3. Effect of using the signed distance preservation term. (a) Image and initialization. (b) Contours around the triangle at levels $\{-80, -40, 0, 40, 80\}$ of converged (179 iterations) level set function with $\gamma = 0$. (c) Contours of converged (136 iterations) level set function using $\gamma = 1$. (d) Zoom on top point of star showing the zero contour for $\gamma = 0$ as the solid line and for $\gamma = 1$ as the dashed line; note that the dashed line is smoother. (e) Contours after convergence using 5 iterations of reinitialization after every 10 level set iterations. For (e), the level set function converged after 124 iterations, implying $12 \times 5 = 60$ iterations of reinitialization. Oscillations are evident in (e) since reinitialization was not applied after final convergence. Parameters were $\tau = 0.05$, $\nu = 0.01 \times 255^2$, and $\lambda_1 = \lambda_2 = 1$.

resulting in a discontinuous, ill-behaved function near the zero level set. Conversely, in (c), we show the same contours using the γ-term. Though true signed distance is not preserved, the level set function is much smoother near the zero contour. Additionally, the resulting contour (dashed line) is smoother as evident in (d). Finally, in (e), we show the resulting contours without using the γ-term but with periodic reinitialization to achieve a result similar to (c).

4.3. Connectivity Preservation

In Fig. 4, we illustrate a potential drawback of topology preserving level sets.[11] As seen in (a), the image comprises a large circle with a small hole near a smaller circle. The contour is initialized inside the large circle. In (b), the resulting segmentation is shown using the traditional algorithm with no topology or connectivity constraints; the result is as expected. In (c) and (d), however, we show the result using topology preservation. Note that significantly more iterations are required to achieve the result in (c) and (d). In (e), we show the result using connectivity preservation, which is achieved in the fewest iterations compared to either the unconstrained or topology preserving method. We do note, however, that the "ideal" result – a single circular contour, without a hole, around the large circle – was achieved by increasing the smoothness parameter from 0.01×255^2 to $\nu = 2.0 \times 255^2$, but required 1351 iterations.

We illustrate further connectivity preservation as compared to topology preservation in Fig. 5 using a spleen likelihood image. In (b), we see the topology preserving result contains many crevices. The connectivity preserving result is shown in (c); it is achieved much more quickly since fewer topology checks were required. We also note the performance improvement provided by the γ-term. Using $\gamma = 0$, the result in (c) required 133 iterations (as opposed to 83) and 54,147 topology checks (as opposed to 22,792).

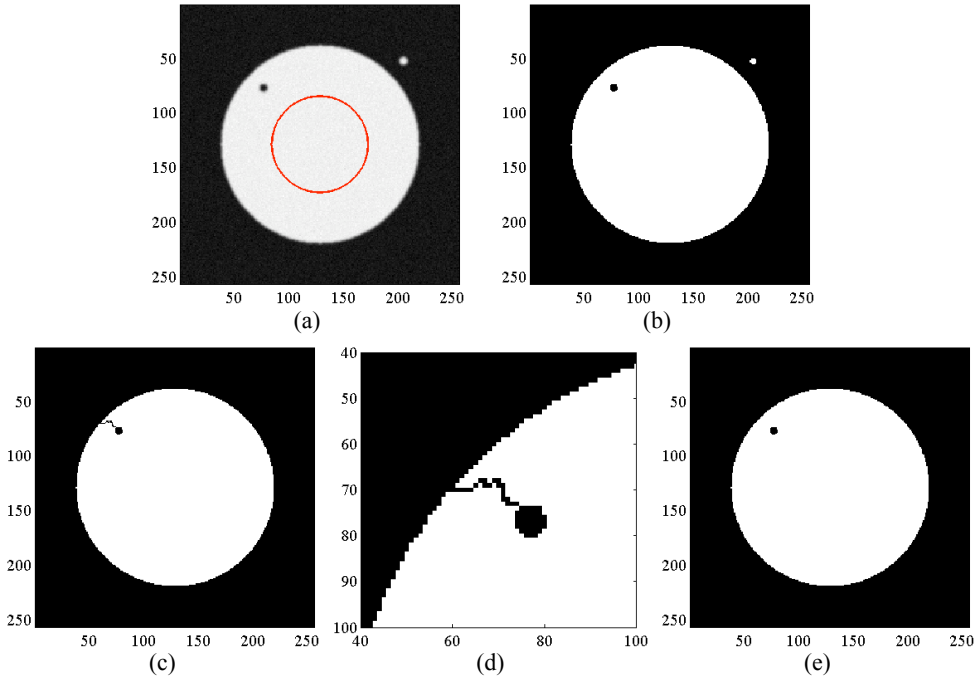

Figure 4. Topology preservation on a phantom comprising a large circle with a hole (top left) near a small circle (top right). (a) Image and initialization. (b) Converged segmentation after 124 iterations without topology or connectivity constraints. (c) Converged segmentation after 179 iterations using topology preservation. (d) Zoom on the hole region from (c). (e) Converged segmentation after 136 iterations using connectivity preservation. Parameters were $\tau = 0.05$, $\nu = 0.01 \times 255^2$, and $\lambda_1 = \lambda_2 = 1$, and $\gamma = 0$.

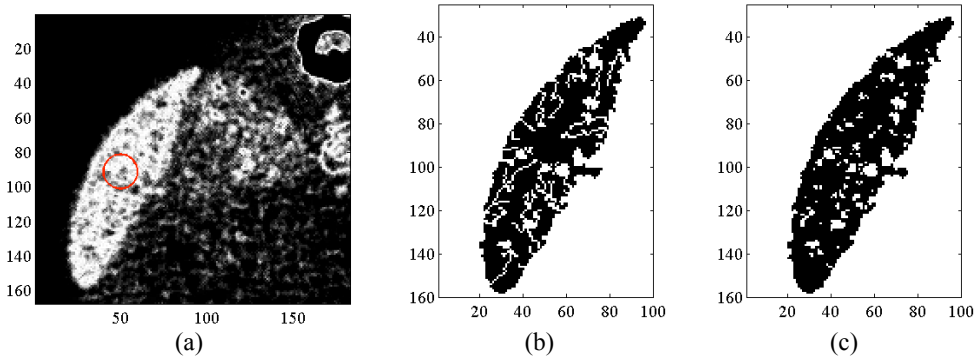

Figure 5. Topology preservation vs. connectivity preservation on spleen likelihood image. (a) Likelihood image and initialization. (b) Topology preserving result in inverse grayscale. Converged after 84 iterations and required 39,953 topology checks. (c) Connectivity preserving result. Converged after 83 iterations and required only 22,792 topology checks. Parameters were $\tau = 0.05$, $\nu = 0.01 \times 255^2$, $\lambda_1 = \lambda_2 = 1$, and $\gamma = 1$. When we used $\gamma = 0$, we note that 133 iterations and 54,147 topology checks were required to achieve the result in (c).

4.4. 3D Results on the Spleen

Here we show some results of fully 3D segmentation, using the likelihood image approach described in Section 3.1, with a data volume of size $174 \times 100 \times 167$. First, in Fig. 6 we show the result without using either the signed distance (γ) term or connectivity preservation. Many disconnected regions in the volume match the blood pool statistics and are hence captured by the segmentation since connectivity is not considered (a similar result is obtained even with $\gamma = 1$). In Fig. 7, we show the much improved result using $\gamma = 1$ and connectivity preservation.

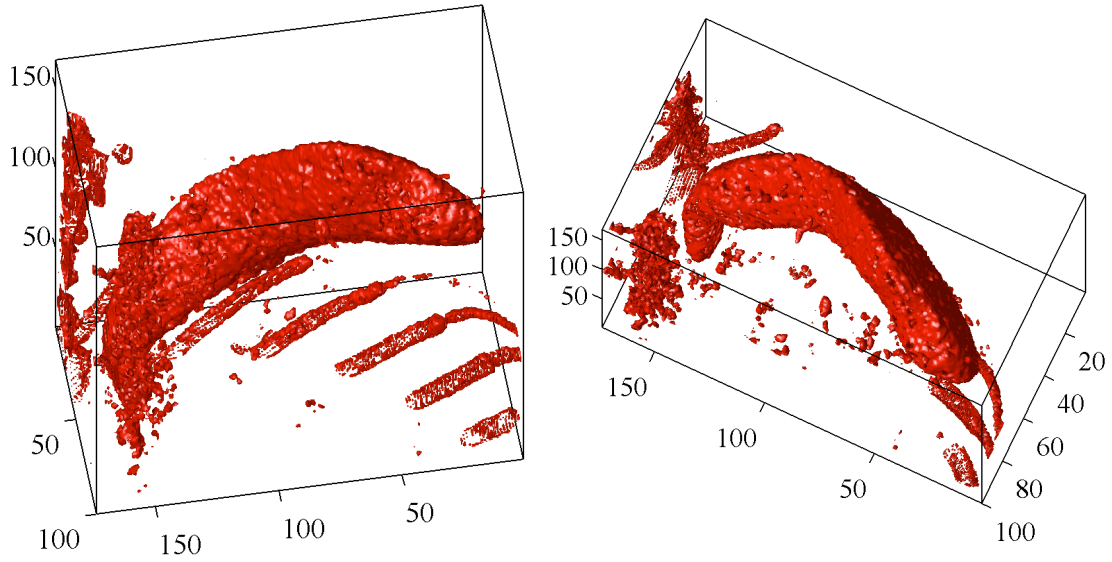

Figure 6. Fully 3D segmentation *without* the signed distance term (i.e., $\gamma = 0$) or connectivity preservation. Parameters were $\tau = 0.05$, $\nu = 0.05 \times 255^2$, and $\lambda_1 = \lambda_2 = 1$. This result was achieved after 500 iterations.

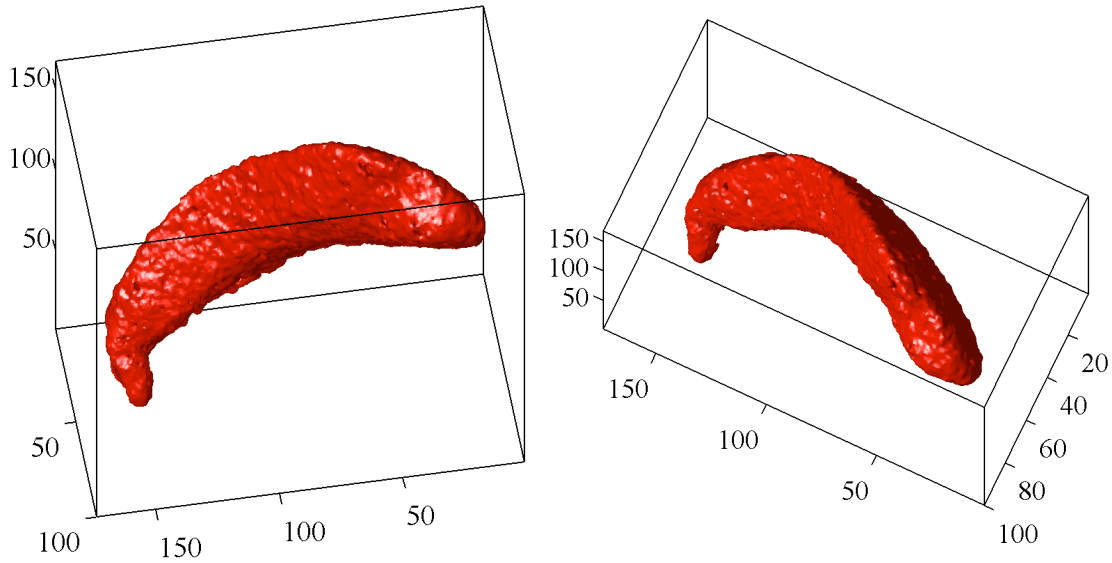

Figure 7. Fully 3D segmentation *with* the signed distance term (i.e., $\gamma = 1$) and connectivity preservation. Parameters were $\tau = 0.05$, $\nu = 0.05 \times 255^2$, and $\lambda_1 = \lambda_2 = 1$. This result was achieved after 500 iterations and required 2,525,334 connectivity checks.

5. CONCLUSIONS

We have presented in this paper several low-level algorithmic improvements to a region-based level set segmentation model. In particular, we integrated the signed distance preserving term of Li *et al.*[5] into the Chan-Vese[6] model and provided formulas for a semi-implicit discretization. We demonstrated the improvement of the semi-implicit scheme over an explicit scheme and also showed how the signed distance preserving term can improve the behavior of the level set function, the smoothness of the final contour, and the speed of convergence. We illustrated that topology preserving level sets can often be problematic and introduced connectivity preservation as an alternative, including experimental results on phantom and real data. We finally showed results on a fully 3D segmentation of the mouse spleen.

Acknowledgements

This work was supported by USPHS Research Grant EB000789 from the National Institute of Biomedical Imaging and Bioengineering and the National Institute of Neurological Disorders and Stroke. Prepared by Oak Ridge National Laboratory, managed by UT-Battelle, LLC, for the U.S. Department of Energy under Contract No. DE-AC05-00OR22725.

REFERENCES

1. National Human Genome Research Institute, "Background on mouse as a model organism." http://www.genome.gov/10005834.
2. J. Wall, S. Kennel, M. Paulus, S. Gleason, J. Gregor, J. Baba, M. Schell, T. Richey, B. O'Nuallain, R. Donnell, P. Hawkins, D. Weiss, and A. Solomon, "Quantitative high-resolution microradiographic imaging of amyloid deposits in a novel murine model of AA-amyloidosis," *Amyloid* **12**(3), pp. 149–156, 2005.
3. J. Price, D. Aykac, and J. Wall, "A 3d level sets method for segmenting the mouse spleen and follicles in volumetric microCT images," in *Proceedings of the IEEE Engineering in Medicine and Biology Conference (EMBC06)*, pp. 2332–2336, 2006.
4. D. Aykac, J. Price, and J. Wall, "3D segmentation of the mouse spleen in microCT via active contours," in *Proceedings of the IEEE Nuclear Science Symposium and Medical Imaging Conference*, **3**, pp. 1542–1545, 2005.
5. C. Li, C. Xu, C. Gui, and M. Fox, "Level set evolution without reinitialization: a new variational formulation," in *Proceedings of the IEEE Computer Society Conference on Computer Vision and Pattern Recognition (CVPR)*, **1**, pp. 430–436, 2005.
6. T. Chan and L. Vese, "Active contours without edges," *IEEE Transactions on Image Processing* **10**(2), pp. 266–277, 2001.
7. S. Osher and J. Sethian, "Fronts propagating with curvature-dependent speed: algorithms based on Hamilton-Jacobi formulation," *Journal of Computational Physics* **79**, pp. 12–49, 1988.
8. G. Papandreou and P. Maragos, "Multigrid geometric active contour models," *IEEE Transactions on Image Processing* **16**(1), pp. 229–240, 2007.
9. M. Sussman, P. Smereka, and S. Osher, "A level set approach for computing solutions to incompressible two-phase flow," *Journal of Computational Physics* **119**, pp. 146–159, 1994.
10. L. Vese and T. Chan, "A multiphase level set framework for image segmentation using the Mumford and Shah model," UCLA CAM Report 01-25, University of California, Los Angeles, 2001.
11. X. Han, C. Xu, and J. L. Prince, "A topology preserving level set method for geometric deformable models," *IEEE Transactions on Pattern Analysis and Machine Intelligence* **25**(6), pp. 755–768, 2003.
12. D. Cremers and S. Soatto, "A pseudo-distance for shape priors in level set segmentation," in *Proceedings of the 2nd IEEE Workshop on Variational, Geometric and Level Set Methods in Computer Vision*, pp. 169–176, 2003.